bond angle (104.6°). The low-frequency limit (398 cm^{-1}) results from the consideration of isolated structures (X_2O molecules), whereas the high-frequency limit (491 cm^{-1}) results from the consideration of the second-order shell of O atoms moving rigidly with C (Si).

13. R. J. Hemley, in *High Pressure Research in Mineral Physics*, M. H. Manghnani and Y. Syono, Eds. (Terra Scientific, Tokyo, 1987), pp. 347–359.
14. S. K. Sharma, J. F. Mammone, M. F. Nicol, *Nature* **292**, 140 (1981).
15. J. D. Jorgensen, *J. Appl. Phys.* **49**, 5473 (1973).
16. T. J. Driscoll and N. M. Lawandy, *J. Opt. Soc. Am.* **B11**, 355 (1994).
17. Y. Sasaki and Y. Ohmori, *Appl. Phys. Lett.* **39**, 466 (1981).
18. In general, the SH of light is generated in noncentrosymmetric crystals, whereas only odd harmonics are observed in centrosymmetric crystals. This stems from the second-order polarization dependence of electromagnetic transitions. In crystals having a center of symmetry, the inversion of all coordinates must leave all relations between physical quantities unchanged. Because the electric field **E** is odd under inversion operations, the polarization field **P** must also be odd, and the coefficients of all even powers in the expansion of the polarization $\mathbf{P} = \varepsilon_o\chi_1\mathbf{E}\sin(\omega t) + \varepsilon_o\chi_2\mathbf{E}^2\sin^2(\omega t) + \varepsilon_o\chi_3\mathbf{E}^3\sin^3(\omega t) + \ldots$ must be 0; ε_o, dielectric constant at ambient conditions; χ, polarizability tensor for medium; ω, frequency of incident light; and t, time. In such crystals, only odd multiples of the incident frequency can be generated.
19. R. W. G. Wyckoff, *Crystal Structures* (Interscience, New York, ed. 2, 1963), vol. 1.
20. S. M. Stishov and V. Popova, *Geochem. Engl. Transl.* **10**, 923 (1961).
21. R. Span and W. Wagner, *J. Phys. Chem. Ref. Data* **25**, 1509 (1996), and references therein.
22. We thank K. Visbeck for experimental assistance and A. McMahan, C. Mailhiot, and M. Nicol for discussions that were valuable to this study. Our x-ray studies were done at the Stanford Synchrotron Radiation Laboratory. This work has been supported by the Laboratory-Directed Research and Development program at the Lawrence Livermore National Laboratory under the auspices of the U.S. Department of Energy under contract W-7405-ENG-48.

23 November 1998; accepted 27 January 1999

Electrostatic Deflections and Electromechanical Resonances of Carbon Nanotubes

Philippe Poncharal,[1] Z. L. Wang,[2] Daniel Ugarte,[3] Walt A. de Heer[1]*

Static and dynamic mechanical deflections were electrically induced in cantilevered, multiwalled carbon nanotubes in a transmission electron microscope. The nanotubes were resonantly excited at the fundamental frequency and higher harmonics as revealed by their deflected contours, which correspond closely to those determined for cantilevered elastic beams. The elastic bending modulus as a function of diameter was found to decrease sharply (from about 1 to 0.1 terapascals) with increasing diameter (from 8 to 40 nanometers), which indicates a crossover from a uniform elastic mode to an elastic mode that involves wavelike distortions in the nanotube. The quality factors of the resonances are on the order of 500. The methods developed here have been applied to a nanobalance for nanoscopic particles and also to a Kelvin probe based on nanotubes.

Ever since their discovery (*1*), carbon nanotubes have been recognized as particularly important nanoscopic systems (*2–9*). The mechanical properties of carbon nanotubes have been the subject of numerous studies (*10–21*). In several experimental studies, the Young's modulus E was found to be extremely high, on the order of 1 TPa (*12*, *14*, *16*, *21*). Theory appears to confirm this value (*10*, *11*, *22*, *23*), which is on the same order as the elastic modulus along the basal plane of highly oriented pyrolythic graphite: $E_a = 1.06$ TPa (*24*). Recent determinations of the Young's modulus rely primarily on rigidity measurements (*25*) and assume that the nanotubes bend by uniform compression of the inner arc of the bent tube and uniform elongation of the outer arc, as for an isotropic rod (*10*). Those measurements either involved electron microscopy–based measurements of thermal vibration amplitudes (*12*) or atomic force microscope (AFM) measurements of cantilevered (*16*) or otherwise suspended (*21*) nanotubes. The arc-produced carbon nanotubes with diameters up to $D = 76$ nm were all found to be rigid, with Young's moduli in the terapascal range. The measurements made to date suffer somewhat from experimental uncertainties such as precise measurements of the thermal vibrational amplitudes, the effect of the AFM tip on the nanotubes, and calibration of the AFM cantilever. Furthermore, they do not give information on the damping of vibrations nor on the shapes of stressed nanotubes.

Here we introduce methods for investigating properties of carbon nanotubes that may be extended into the mesoscopic size range. We used those methods on arc-produced, multiwalled carbon nanotubes (MWNTs) (*26*). The technique relies on resonant excitation of selected carbon nanotubes in situ in a transmission electron microscope (TEM) (*27*). In these experiments, we attached a fiber composed of carbon nanotubes (which was recovered from the nanotube arc deposit) to a fine gold wire (*7*). The wire was mounted on a small electrically insulated support so that a potential could be applied to it. This assembly was inserted in a custom-built specimen holder of the TEM in such a way that the fiber was about 5 to 20 μm away from a grounded counterelectrode. The specimen holder was provided with a piezo-driven translation stage and a micrometer-driven translation stage to accurately position the fiber relative to the counterelectrode. To accurately measure the length L and diameter D of the investigated nanotube, the sample holder could be rotated about its axis so that the nanotube under investigation could be aligned perpendicular to the electron beam.

When a static potential V_s was applied to the wire, the carbon nanotubes that protruded from the fiber became electrically charged and were attracted to the counterelectrode. The nanotubes that were not perpendicular to the counterelectrode bent toward it (Fig. 1). We compared the shape of the bent nanotube to that of a cantilevered elastic beam when a force was applied to its tip and also to that of a beam with a uniformly distributed force. This analysis demonstrated that the force exerted on the nanotube is essentially entirely at the tip, hence the charge should be located there. [This result is expected from classical electrostatics applied to conducting needle-shaped conductors (*28*).] Furthermore, the measured deflection is proportional to V_s^2 [after taking into account a slight voltage offset (Fig. 1C)]. This is to be expected for a nanotube that follows Hook's law, because the force equals the product of the induced electric charge (proportional to V_s) and the electric field (also proportional to V_s). Hence, if the charge on the tip equals αV_s, where α is a nanotube-dependent constant that depends on the geometry, and if the electric field is βV_s, then the static force at the tip is $F_s = \alpha\beta V_s^2$. Small deflections are proportional to F_s. In the course of these measurements, we found that a nanotube with $D = 20$ nm can be bent to a radius of curvature at least as small as 80 nm, after which it returns to its original straight configuration, which indicates that such extreme bending does not exceed the elastic limit (*14*, *19*).

Application of a time (t)-dependent voltage to the nanotubes [$V(t) = V_d\cos(\omega t)$]

---

[1] School of Physics, Georgia Institute of Technology, Atlanta, GA 30332–0430, USA. [2] School of Materials Science and Engineering, Georgia Institute of Technology, Atlanta, GA 30332–0245, USA. [3] Laboratório National de Luz Síncrotron, Cx Postal 6192, 13083–970 Campinas SP, Brazil.

*To whom correspondence should be addressed.

caused a time-dependent force and dynamic deflections (the forces are described in Eq. 2). Adjustment of the angular frequency $\omega = 2\pi\nu$ allowed the nanotubes to be resonantly excited, which caused large-amplitude deflections for relatively small excitation voltages V_d. For example, for the vibrations in Fig. 2B, $V_d = 100$ mV and the frequency $\nu_1 = 530$ kHz. The shape of the dynamically deflected nanotube (which is independent of the details of the force distribution on the nanotube) corresponds to the shape predicted for a resonantly excited cantilevered beam. The frequencies are found from the following equation (*29*)

$$\nu_j = \frac{\beta_j^2}{8\pi}\frac{1}{L^2}\sqrt{(D^2 + D_i^2)}\sqrt{\frac{E_b}{\rho}} \qquad (1)$$

where D is the outer diameter, D_i is the inner diameter, E_b is the elastic modulus, ρ is the density, and β_j is a constant for the jth harmonic: $\beta_1 = 1.875$, $\beta_2 = 4.694$. This equation results from the Bernoulli-Euler analysis of cantilevered elastic beams (*29*). If the beam bends by elongation of the outer arc and a compression of the inner arc of the bend, then E_b can be identified with the Young's modulus E of the material (*29*). However, to retain generality, we will call this constant the effective bending modulus E_b, for the reasons given below.

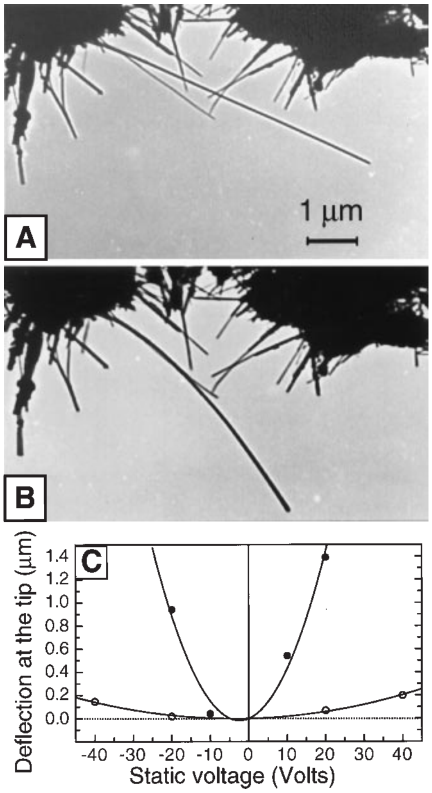

Fig. 1. Electron micrographs of the electromechanical deflections of a carbon nanotube. (**A**) Uncharged nanotube ($V_s = 0$). (**B**) Charged nanotube ($V_s = 20$ V). Here an electrical potential difference was applied between the nanotube (which was connected to a nanotube fiber) and a counterelectrode (not shown). The charge induced on the nanotube interacted with the electric fields between the nanotube and the counterelectrode and resulted in an attractive force, which caused the nanotube to bend. An analysis of the shape of the bent nanotube showed that essentially all of the induced charge was at the tip of the nanotube. The bending process was reversible even for extreme bends (with radii of curvature <100 nm), which indicates the large elastic strength of the nanotubes. (**C**) Measured static deflections as a function of V_s for two nanotubes (solid circles: $D = 18$ nm, $L = 4.6$ µm; open circles: $D = 41$ nm, $L = 1.5$ µm), showing the quadratic dependence on V_s. The slight voltage offsets of the minima of the fitted parabola are attributed to work function effects (see also Fig. 4).

Higher modes can be excited, such as the second harmonic of the same nanotube (Fig. 2C). The frequency of this vibration is $\nu_2 = 3.01$ MHz $= 5.68\ \nu_1$. For a uniform cantilevered beam, the theoretical ratio $\nu_2/\nu_1 = 6.2$ (*29*). The position of the node in the ν_2 mode is found at 0.76 L, which is very close to the theoretical value of 0.8 L (*29*). Although a detailed analysis of the sequence of harmonics combined with an analysis of the deflected contours can provide detailed information on individual nanotubes, we have chosen to concentrate on trends in the elastic moduli with nanotube diameter. The resonant frequencies may drift very slightly with time (either positively or negatively). However, we have not found evidence for irreversible changes to the nanotubes. Even when a large-amplitude resonant vibration was applied to a nanotube for 30 min (>10^9 cycles), the frequency drift was less than 1%.

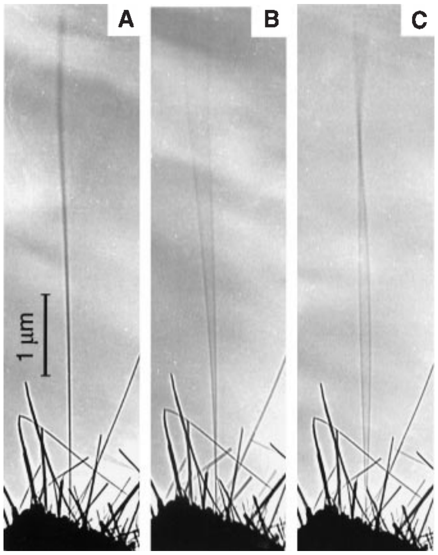

Fig. 2. Nanotube response to resonant alternating applied potentials. (**A**) In the absence of a potential, the nanotube tip ($L = 6.25$ µm, $D = 14.5$ nm) vibrated slightly because of thermal effects. Although thermal amplitude is difficult to evaluate, it was nevertheless used to measure the Young's modulus in a previous study (*12*). (**B**) Resonant excitation of the fundamental mode of vibration ($\nu_1 = 530$ kHz); the shape corresponds closely to that expected for a cantilevered uniform beam. The high contrast at the extremes of the oscillations is caused by the relatively long times spent at the turning points [compare with (A)]. (**C**) Resonant excitation of the second harmonic ($\nu_2 = 3.01$ MHz). Both the frequency and the shape correspond reasonably well to that expected for this harmonic. For this nanotube, $E_b = 0.21$ TPa.

Figure 3 shows the E_b for several MWNTs determined from measurements of ν_1, D, and L (*30*). Several values from other sources are superimposed. It is clear that E_b is very large (≈1 TPa) for $D < 10$ nm, and that E_b drops dramatically to lower values ($E_b \approx 100$ GPa) for tubes of larger diameter. For small D, our measurements correspond well with those found by others, but for larger D our values are significantly lower than those found in (*16*).

Such a great reduction in E_b must be related to the emergence of another bending mode of the nanotube. Most likely, this mode corresponds to the wavelike distortion or ripple on the inner arc of the bent nanotube that is observed for slightly bent, relatively thick nanotubes (*11*, *20*). A particularly clear example is shown in Fig. 3D (*31*). The ripple structure in the tube 31 nm in diameter caused the nanotube to bend uniformly, with a radius of curvature from ≈400 nm, which is only a factor of 3 smaller than typical curvatures in the resonant experiments described here. The amplitude of the ripple increased uniformly from essentially 0 for layers near the center of the nanotube to about 2 to 3 nm for the outer layers. There were no discontinuities in consecutive interlayer spacings nor was there evidence of defects. Ripple amplitude increased continuously and smoothty with decreasing nanotube curvature. In contrast, a thin slightly bent nanotube (8 nm in diameter) did not present ripples for a 300-nm radius of curvature, but the same tube did show evidence for buckling (*32*) and damage on sections where the radius of curvature was decreased to 24 nm (*11*, *19*).

The appearance of the ripples is most likely related to the consequent reduced compression of the carbon bonds of the inner arc of the bend as compared with uniform bending. This process causes a large reduction in the strain energy associated with the Young's modulus parallel to the basal plane of graphite (for bulk graphite, $E_a = 1.06$ TPa). The rippling mode is likely to be energetically favorable (at least for large diameter tubes), because the other four elastic moduli for bulk graphite are all much smaller than E_a (*33*). However, a detailed theoretical analysis will be required to explain the crossover from the uniform (compression/elongation) mode to the rippling mode.

Defects that cross-link adjacent nanotube layers could prevent this rippling effect and thereby cause the nanotubes to retain their large E_b. This mechanism could then explain discrepencies between our measurements and those of others (*16*) and is reminiscent of work hardening in metals, which causes soft metals to become harder because of crystallographic defects. This hypothesis is supported by preliminary results that showed that 200-keV electron irradiation caused the resonance frequencies to increase. Electrons with these energies (in contrast to the 100-keV electrons used in this work) are known to damage graphitic structures (*34*).

The dependence of the amplitude on frequency (for constant V_d) shown in Fig. 3 (inset) is approximately Lorentzian, as expected for damped harmonic vibrations. The full width at half maximum $\Delta\nu/\nu = 6 \times 10^{-3}$ corresponds to a quality factor $Q = 170$ for the resonance of this nanotube ($E_b = 0.098$ TPa). Larger Qs were observed for tubes that exhibited larger E_b (for example, $Q = 500$, $E_b = 0.73$ TPa). We have not observed shifts in the resonance frequencies for large-amplitude vibrations, which indicates that the response remains linear for large-amplitude deflections and for all measured Ds.

The rippling mode is linear and its properties are well described by the Bernoulli-Euler analysis (*29*). The correct prediction of the frequency ratio ν_2/ν_1 is further strong evidence that bending does not involve kink formation. Nevertheless, the reduction by an order of magnitude in the rigidly of the nanotube certainly shows the dramatic effect of this mode on the elastic properties. The rippling mode appears to be more damped than the uniform mode, which may be due to increased internal friction (*24*). However, there is no evidence for hysteresis or nonlinear response in this mode, which sets it apart from the buckling instability (*13*, *14*, *19*).

The resonance methods developed here can be applied to determine various other properties of carbon nanotube systems. For example, in general a static charge is present on opposing electrodes of different materials, even when both electrodes are in mutual electrical contact and at ground potential (*35*). These charges can be neutralized by applying the appropriate bias voltage ΔV between the electrodes, which is related to the work functions of the materials involved. This well-known effect is used, for example, in the Kelvin probe method (*36*) to determine work functions and can be used analogously in the present configuration. If a constant voltage offset V_s is supplied to the time-dependent voltage, then $V(t) = V_s + V_d \cos(\omega t)$. Consequently, the charge on a nanotube is $q = \alpha[\Delta V + V(t)]$ and so $F(t) = \beta[\Delta V + V(t)]q$, where α and β are nanotube specific. The general expression for the force on a nanotube is given by

$$
\begin{aligned}
F(t) &= \alpha\beta[\Delta V + V_s + V_d\cos(\omega t)]^2 \\
&= \alpha\beta[(\Delta V + V_s)^2 \\
&\quad + 2(\Delta V + V_s)V_d\cos(\omega t) \\
&\quad + \frac{1}{2}V_d^2\cos(2\omega t) + \frac{1}{2}V_d^2] \qquad (2)
\end{aligned}
$$

One of the two time-dependent terms in the force oscillates at the driving frequency, which scales linearly with V_d, whereas the other is at twice this frequency and scales as V_d^2. The linear term contributes to the force even when $V_s = 0$ (*37*). We have identified both the linear and the quadratic response through their characteristic voltage dependences (and frequency ratios). In particular, a plot of the vibration amplitude at resonance as a function of V_s shows a linear dependence in the linear mode (Fig. 4B). This property distinguishes it from the quadratic mode, which is insensitive to V_s.

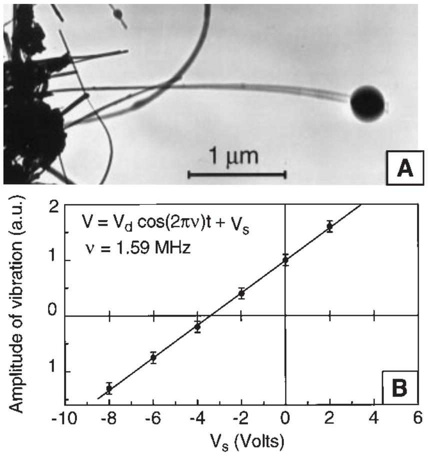

Fig. 4. Further applications of the resonant method described here. (**A**) Resonance vibrations of a nanotube loaded with a spheroidal carbon particle. From the resonance frequency $\nu = 968$ kHz, the mass of this particle is determined to be $M = 22 \pm 6$ fg. $E_b = 90$ GPa for this 42-nm-diameter nanotube (see Fig. 3), so that the calculated unloaded resonant frequency of the tube is 3.28 MHz. The calculated mass of this 308-nm-diameter particle is $M \approx 30$ fg, assuming spherical geometry and bulk density. This nanobalance technique is a direct way to weigh individual particles in the femtogram-to-picogram size range. (**B**) Plot of the amplitude of vibration of a nanotube at resonance with the static bias voltage V_s, which demonstrates the predicted linear dependence and the voltage offset ΔV due to work function effects. Error bars indicate errors in measuring the vibration amplitude.

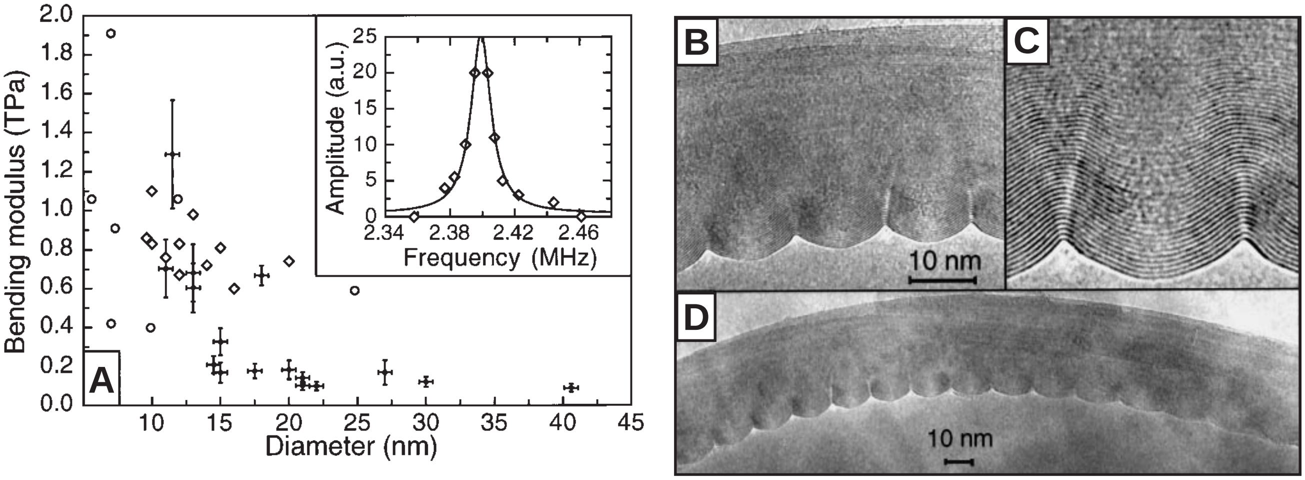

Fig. 3. Elastic properties of nanotubes. (**A**) E_b as a function of diameter: solid circles, present data; diamonds, data from (*21*); open circles, data from (*12*). [A further data point at $D = 32.9$ nm and $E_b = 1.26$ TPa from (*16*) is obscured by the inset.] Error bars indicate absolute error in L and D; the error in the resonant frequency is negligible. The dramatic drop in E_b for $D \approx 12$ nm is attributed to the onset of a wavelike distortion, which appears to be the energetically favorable bending mode for thicker nanotubes. There is no remarkable change in the Lorentzian line shape of the resonance (**inset**) for tubes that have large or small moduli, although the low-modulus nanotubes appear to be more damped than the high-modulus tubes. (**D**) High-resolution TEM image of a bent nanotube (radius of curvature ≈ 400 nm), showing the characteristic wavelike distortion. (**B** and **C**) Magnified views of a portion of (D). The amplitude of the ripples increases continuously from the center of the tube to the outer layers of the inner arc of the bend. Note the absence of discontinuities in the interlayer spacing.

The intercept of the line with the abscissa yields ΔV. This geometry-independent constant is characteristic for the specific nanotube under investigation and is typically on the order of several volts. Similarly, attaching nanoscopic conducting particles to the nanotubes facilitates measurements of their work functions.

The methods developed here are also well suited to measure masses in the picogram-to-femtogram mass range, as demonstrated in Fig. 4A, which shows the resonance of a carbon particle that is attached to the end of a nanotube (38). The mass of this particle was determined from the resonance frequency of the structure and was found to be $M = 22 \pm 6$ fg (1 fg = 10^{-15} g). This value is near that calculated from the measured geometry, assuming bulk amorphous carbon density—that is, $M \approx 30$ fg. This nanobalance method can be applied to other particles of similar dimensions, such as viruses.

References and Notes

1. S. Iijima, *Nature* **354**, 56 (1991).
2. J. W. Mintmire, B. I. Dunlap, C. T. White, *Phys. Rev. Lett.* **68**, 631 (1992).
3. M. S. Dresselhaus, G. Dresselhaus, R. Saito, *Carbon* **33**, 883 (1995).
4. D. L. Carroll *et al.*, *Phys. Rev. Lett.* **78**, 2811 (1997).
5. T. W. Ebbesen, *Phys. Today* **49**, 26 (1996).
6. W. A. de Heer, A. Chatelain, D. Ugarte, *Science* **270**, 1179 (1995).
7. S. Frank, P. Poncharal, Z. L. Wang, W. A. de Heer, *ibid.* **280**, 1744 (1998).
8. J. Liu *et al.*, *ibid.*, p. 1253.
9. A. Thess *et al.*, *ibid.* **273**, 483 (1996).
10. D. H. Robertson, D. W. Brenner, J. W. Mintmire, *Phys. Rev. B* **45**, 12592 (1992).
11. R. S. Ruoff and D. C. Lorents, *Carbon* **33**, 925 (1995).
12. M. M. Treacy, T. W. Ebbesen, J. M. Gibson, *Nature* **38**, 678 (1996).
13. B. I. Yakobson, C. J. Brabec, J. Bernholc, *Phys. Rev. Lett.* **76**, 2511 (1996).
14. M. R. Falvo *et al.*, *Nature* **389**, 582 (1997).
15. J. P. Lu, *Phys. Rev. Lett.* **79**, 1297 (1997).
16. E. Wong, P. Sheehan, C. Lieber, *Science* **277**, 1971 (1997).
17. C.-H. Kiang *et al.*, *Phys. Rev. Lett.* **81**, 1869 (1998).
18. W. H. Knechte *et al.*, *Appl. Phys. Lett.* **73**, 1961 (1998).
19. S. Iijima, C. Brabeck, A. Maiti, J. Bernholc, *J. Chem. Phys.* **104**, 2089 (1996).
20. T. Kuzumaki *et al.*, *Phil. Mag. A* **77**, 1461 (1998).
21. J.-P. Salvetat *et al.*, *Adv. Mat.*, in press.
22. N. Yao and V. Lordi, *J. Appl. Phys.* **84**, 1939 (1998).
23. G. Gao, T. Cagin, W. A. Goddard, *Nanotechnology* **9**, 184 (1998).
24. B. T. Kelly, *Physics of Graphite* (Applied Science, London, 1981).
25. N. Osakabe *et al.*, *Appl. Phys. Lett.* **70**, 940 (1997).
26. T. W. Ebbesen and P. M. Ajayan, *Nature* **358**, 220 (1992). We caution that different production recipes can yield different results; in particular, defect densities may vary substantially from one laboratory to the next (as is the case with crystal growing). For example, catalytically grown tubes are usually very defective. In contrast, the nanotube material used in this work [including (*31*)] was from the same stock as was used in our previous work (*6*, *7*) and was of high quality.
27. The TEM used was a JEOL 100C (100 kV) at the School of Materials Science and Engineering, Georgia Institute of Technology.
28. D. J. Griffiths and Y. Li, *Am. J. Phys.* **64**, 706 (1996).
29. L. Meirovich, *Elements of Vibration Analysis* (McGraw-Hill, New York, ed. 2, 1986).
30. D_i was not measured for all nanotubes, and in those cases it was not included in the calculations. However, the value for E is rather insensitive to D_i, because $D_i/D = 1/4$, which is an extreme case, differs only by 7% as compared with $D_i = 0$.
31. Microscopy was performed with a Philips CM30 200-kV high-resolution TEM.
32. The ripple mode may be a precursor to buckling, but it should not be confused with bucking. Buckling (in contrast to rippling) is characterized as an instability giving rise to a nonlinear response. It occurs in highly stressed nanotubes (and beams) and manifests as one or several kinks with very small radii of curvature (about 1 to 10 nm). It is accompanied by abrupt change in the effective force constant and may cause irreversible damage. The observed effect may be related to the rippling found in classical beams as a precursor to buckling [see S. Kyriakides and G. T. Ju, *Int. J. Solids Struct.* **29**, 1117 (1992)].
33. In the bulk, the other elastic moduli are at least a factor of 5 and as much as a factor of 50 smaller than that of C_{11}.
34. D. Ugarte, *Nature* **352**, 707 (1992).
35. Lord Kelvin, *Philos. Mag.* **46**, 82 (1898).
36. N. A. Sulpice and R. J. D'Arcy, *J. Phys. E* **3**, 477 (1970).
37. Electrical charging due to the electron beam cannot account for the effect, because the charge found to reside on the nanotubes is positive rather than negative. Furthermore, the amplitude of vibration at resonance does not change with electron dose, as it would if electron beam charging were important.
38. M. Gurgoze, *J. Sound Vib.* **190**, 149 (1996).

39. We thank U. Landman, R. L. Whetten, L. Forro, and A. Zangwill for fruitful discussion and R. Nitsche for his analysis of the static bent nanotube. D.U. thanks the Centre Interdepartemental de Microscopy Electronique, Ecole Polytechnique Federale, for the use of the Philips CM30 microscope for Fig. 3, B through D, and the Brazilian Council for Scientific and Technological Research. Supported by the Army Research Office, grants DAAG 55-97-0133 (W.A.d.H. and P.P.), by NSF9733160 (Z.L.W.), and by NSFDMR-9971412 (W.A.d.H. and Z.L.W.)

4 December 1998; accepted 26 January 1999

An Elusive Blind-Thrust Fault Beneath Metropolitan Los Angeles

John H. Shaw[1]* and Peter M. Shearer[2]

Seismic reflection profiles, petroleum wells, and relocated earthquakes reveal the presence of an active blind-thrust fault beneath metropolitan Los Angeles. A segment of this fault likely caused the 1987 Whittier Narrows (magnitude 6.0) earthquake. Mapped sizes of other fault segments suggest that the system is capable of much larger (magnitude 6.5 to 7) and more destructive earthquakes.

Damages exceeding \$35 billion from the 1994 Northridge [magnitude (M) 6.7] earthquake (1), combined with recent evidence of larger ($>M$ 7) events in the geologic record (2), have focused attention on the hazards posed by thrust faults to metropolitan Los Angeles. Efforts to assess and mitigate these hazards are complicated, however, because thrust faults beneath the city are typically blind, meaning that they lie concealed beneath Earth's surface (3, 4). Here, we used high-resolution, subsurface images acquired by the petroleum industry (Fig. 1) and relocated seismicity to map a large blind-thrust system lying directly beneath the metropolitan area (Fig. 2).

Many blind thrusts produce near-surface folds that grow during repeated earthquakes (3–5) in response to motions through bends in fault planes or above propagating fault tips, and their shapes reflect underlying fault geometries and slip (6, 7). Seismic reflection profiles and information from oil wells reveal a series of these anticlines extending from downtown Los Angeles to the Coyote Hills (8–10) in northern Orange County (Fig. 2). These folds grew in the Quaternary while sediments were deposited above them, yielding patterns of deformed strata that record fold growth and fault slip (11). These deformed strata are particularly well imaged in the Santa Fe Springs anticline (Fig. 1).

On the basis of fault-related folding theories (11), the shape of the growth fold at Santa Fe Springs suggests that an underlying fault, which we call the Puente Hills thrust, dips to the north and extends upward into the Pliocene Fernando Formation. This fault shape and position are consistent with a north-dipping reflection beneath the anticline that cuts across bedding. This reflection is observed on more than 10 seismic profiles and persists through a range of processing steps aimed to remove noise and artifacts (12). Thus, we interpret this reflection as an image of the fault surface, caused by velocity and density contrasts that exist across the fault plane.

Fault-plane reflections in a series of seismic profiles define an east-west–striking surface that dips about 27° to the north. We extrapolated beyond the limits of the fault-plane reflections, using fold shape, as imaged in the seismic profiles, to predict the fault shape (6, 11) and map the fault surface (Fig. 2). The mapped fault extends 40 km along strike and includes three distinct geometric

---

[1] Department of Earth and Planetary Sciences, Harvard University, Cambridge, MA 02138, USA. [2] Institute of Geophysics and Planetary Physics, Scripps Institute of Oceanography, University of California, San Diego, La Jolla, CA 92093–0225, USA.

*To whom correspondence should be addressed. E-mail: shaw@eps.harvard.edu